Transient Angle Stability of Inverters Equipped with Robust Droop Control

Chen Qi, Keyou Wang, Member, IEEE, Qing-Chang Zhong, Fellow, IEEE, Jin Xu, and Guojie Li, Senior Member, IEEE

Abstract—Transient angle stability of inverters equipped with the robust droop controller is investigated in this work. At first, the conditions on the control references to guarantee the existence of a feasible post-disturbance operating point are derived. Then, the post-disturbance equilibrium points are found and their stability properties are characterized. Furthermore, the attraction regions of the stable equilibrium points are accurately depicted by calculating the stable and unstable manifolds of the surrounding unstable equilibrium points, which presents an explanation to system transient stability. Finally, the transient control considerations are provided to help the inverter ride-through the disturbance and maintain its stability characteristics. With these, it is shown that the transient angle stability is not a serious problem for droop controlled inverters with proper control settings.

Index Terms—transient angle stability, droop controlled inverter, equilibrium point, (un)stable manifold

I. Introduction

The utilization of renewable energy generations to support electric loads is gradually shifting the paradigm of power systems [1], [2]. Since most of these renewable energy generations are connected into the grids through inverters, it can be predicted that an increasing number of inverters will be added into the power system and greatly affect its operating characteristics [3]. Therefore, the operation properties of inverters should be carefully studied [4].

Specifically, the control technique and stability analysis of inverters are usually discussed, which are also interrelated themselves. As a power electronic device, the dynamic characteristics of the inverter are mainly influenced by its controller, which further plays a very important role in determining the stability of the system. Among different control techniques, the droop controller has been well recognized by researchers because of its ability to work in a decentralized way [5], [6], to actively support the system [7], [8] and to autonomously synchronize with the grid [9], [10]. Over recent years, lots of attention has been paid to the improvements and applications of the droop controller, whereas the stability problem has also been discussed.

The stability issues in the power system can be classified as small-disturbance stability and large-disturbance stability [11]. Compared to the former category, the large-disturbance stability is much less studied for inverters, probably because they are usually immediately tripped off once a large disturbance is detected, such as when a fault occurs. However, with more

This work was supported in part by National Natural Science Foundation of China (No. 51877133), China Scholarship Council, and National Science Foundation (Award No. 1810105).

C. Qi, K. Wang, J. Xu and G. Li are with the Key Laboratory of Control of Power Transmission and Conversion, Ministry of Education, Shanghai Jiao Tong University, Shanghai, 200240, China. (corresponding authors: Jin Xu, xujin20506@qq.com, Keyou Wang, wangkeyou@sjtu.edu.cn)

Q-C. Zhong is with the Department of Electrical and Computer Engineering, Illinois Institute of Technology, Chicago, Illinois, 60616, USA.

inverters equipped with the fault ride-through capability [12], [13], attention should also be paid to this kind of stability. It should be noticed that according to the definition in [11], the term *transient stability* is used to specify the *rotor angle stability* of the synchronous generator, which is contrasted to the *voltage stability*. Similarly, the *power angle stability* is investigated for the droop controlled voltage source inverters in this work, and the term *transient stability* is inherited to indicate the system stability after a large disturbance.

Conventionally, transient stability is usually studied using the time-domain simulation method or the direct method, including the Lyapunov-based methods [14], the extended equal area criterion [15] and so forth. Following these routes, some researchers investigated the transient stability of the inverters with droop control. For example, time-domain simulations were carried out in [16], which concluded that the transient stability problem of droop controlled inverters does not need to be worried about, but further explanations were not provided. By contrast, theoretical analyses were conducted in some other works. An energy function was constructed in [17] by making the droop controlled inverter model similar to the classic second-order synchronous generator model. Lyapunov functions were given in [18] using the Takagi-Sugeno multi-modeling method, where the estimated attraction regions were compared regarding the inverter models with different orders. And the idea from equal area criterion was applied in [19] to analyze the synchronous instability mechanism of droop controlled inverters when the current was saturated under transient events. However, it is still an open question to accurately and completely characterize the transient stability of the droop controlled inverter.

In addition to following the routes used in the conventional power system studies, researchers also tried to solve the problem from other perspectives. The works in [20]–[23] gave several conditions regarding the transient stability and synchronization of the droop controlled inverter by introducing the concepts and techniques in control and system theories, including the generalized Kuramoto model, the port-Hamiltonian system, and the Kalman-Yakubovich-Popov condition. These works provided mathematically rigorous analyses, but the difficulty was also increased to understand the physical significance behind this problem from the complicated mathematical derivations.

Compared to the existing works, this paper aims to provide some insights about the transient stability of the inverters equipped with droop mechanism. Essentially speaking, transient stability investigates whether the system is able to return to a proper operating point after a large disturbance is cleared and the system restores its normal topology and control, which refers to the post-disturbance system [24]. Therefore, the most intrinsic approach for this problem is to find the accurate stability region of the post-disturbance system and analyze the stability consider-

1

ing the system trajectory. This idea motivates the studies in this paper. In this work, the robust droop controller (RDC) [4], [25] is taken as an example to operate the inverter, and its transient stability characteristics are studied in a single machine infinite bus (SMIB) scenario by first obtaining the stable equilibrium points (SEPs) and unstable equilibrium points (UEPs) of the system, and then depicting the attraction regions of the SEPs. The contributions of this work include:

- Firstly, a feasible operation region is derived for the control references of the droop controlled inverter, which serves as the prerequisite for the system transient stability.
- Then, a good transient angle stability characteristic of the droop controlled inverter is revealed, which means a SEP can always be found by the post-disturbance system and a stable final state can always be obtained.
- Finally, the transient control considerations are provided regarding the current limiting and the reverse active power prevention, which further help the droop controlled inverter maintain its stability characteristics.

The rest of this paper is organized as follows. The studied system model is introduced in Section II. The feasible operation region for the control references is derived in Section III to guarantee the existence of feasible SEPs. The characterization of the system equilibrium points is analyzed in Section IV. The accurate attraction regions of the SEPs are depicted and verified in Section V to understand the system transient stability properties. The transient control considerations regarding the current limiting and reverse active power prevention are discussed in Section VI. And the conclusions are made in Section VII.

II. SYSTEM MODEL

Although the droop control is usually adopted where multiple inverters are parallel connected, it is clearer to reveal the internal mechanism of transient angle stability in a classical SMIB scenario, and thus, the SMIB system is considered in this work.

Table I VALUES OF SYSTEM PARAMETERS.

Symbol	Explanation	Value
V_g	grid voltage RMS value (line-line)	100 V
ω_g	grid voltage angular speed	$100\pi\mathrm{rad/s}$
R_g	grid side resistance	0.1Ω
L_g	grid side inductance	$0.5\mathrm{mH}$
R_l	line resistance	0.1Ω
L_l	line inductance	$0.5\mathrm{mH}$
R_s	LC filter resistance	0.1Ω
L_s	LC filter inductance	$2\mathrm{mH}$
C_s	LC filter capacitance	$20\mu\mathrm{F}$
R_f	fault ground resistance	0.01Ω

Both the steady-state and dynamic models of the discussed system will be derived in this section. For a better presentation, one set of system and control parameters are given in Tables I and II as an example, and some of the illustrations in the following sections are carried out with these parameters.

In this work, the system parameters are selected to operate the inverter in a relatively weak system, where the transient angle stability problem is expected to be a more serious threat. On the other hand, the droop coefficients are set that when the system frequency deviates $0.5\,\mathrm{Hz}$ (1% of the rated frequency), the inverter will provide $1000\,\mathrm{W}$ active power regulation (20%

Table II Control parameters of the inverter.

Symbol	Explanation	Value
S_{base}	inverter base capacity	5000 VA
$V_{base}^{line, rms}$	voltage base (line-line RMS)	$100\mathrm{V}$
P_{set}	active power reference	$4000 { m W}$
Q_{set}	reactive power reference	3000 Var
ω^*	angular speed reference	$100\pi\mathrm{rad/s}$
E_r	inverter voltage reference	100 V
m	active power droop coefficient	$0.001\pi (W \cdot s)^{-1}$
n	reactive power droop coefficient	$0.25\mathrm{V/var\cdot s}$
K_e	inverter voltage droop coefficient	$50 {\rm s}^{-1}$

of the capacity), and when the voltage deviates $5\,\mathrm{V}$ (5% of the rated voltage), the inverter will provide $1000\,\mathrm{Var}$ reactive power regulation (20% of the capacity). It should be noticed that these specific parameters shown in Tables I and II are adopted only to present the analysis more clearly. However, the conclusions of this work have been validated under a wide range of parameters through extensive simulations.

Furthermore, from the perspective of engineering practice, the inverter control parameters can be designed by first selecting the droop coefficients m, n and K_e according to the requirements on the inverter to support system frequency and voltage, which should also be reasonable regarding the capacity of the inverter. Then the control references P_{set} , Q_{set} , and E_r can be further determined considering the dispatch instructions and the conditions proposed in Section III of this work.

A. Description of the SMIB System

The studied SMIB system is shown in Fig. 1. The infinite bus is modeled as an ideal voltage source $V_g \angle 0$. And the inverter is modeled as a controllable voltage source $E \angle \delta$, where δ is the power angle with respect to the infinite bus. Since the transient stability is investigated after a large disturbance, a three-phase ground fault is applied at bus 2 which has a ground resistance R_f . In this work, it is assumed that the fault is cleared by itself with no line tripped and therefore, the post-disturbance system topology is the same as the pre-disturbance one.

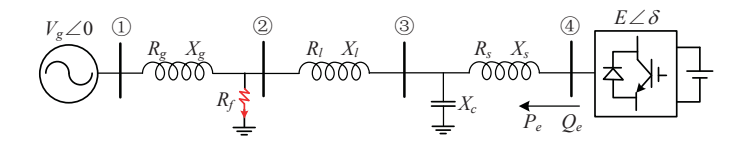


Figure 1. The discussed SMIB system.

This complete system can be further reduced to a compact 2-bus system using the well-known Kron reduction [26], and the reduced system includes only the grid bus and inverter bus. The steady-state model of the reduced system is represented as (1).

$$\begin{bmatrix} I_g \angle \varphi_g \\ I_e \angle \varphi_e \end{bmatrix} = \underbrace{\begin{bmatrix} G_{11} + jB_{11} & G_{12} + jB_{12} \\ G_{21} + jB_{21} & G_{22} + jB_{22} \end{bmatrix}}_{\mathbf{Y}_{und}} \begin{bmatrix} V_g \angle 0 \\ E \angle \delta \end{bmatrix} \tag{1}$$

where $V_g \angle 0$ and $E \angle \delta$ are respectively the grid voltage and inverter voltage. $I_g \angle \varphi_g$ and $I_e \angle \varphi_e$ are respectively the grid current and inverter current. \boldsymbol{Y}_{red} is the complex admittance matrix of the reduced system, where its real parts and imaginary

parts are respectively G_{ij} and B_{ij} (i,j=1 or 2). It should be noticed that since the transient stability is usually discussed regarding the post-disturbance system, \boldsymbol{Y}_{red} and its elements G_{ij} and B_{ij} are referred to the post-disturbance system parameters by default in this work.

B. Inverter Dynamic Model

In this study, the inverter is modeled as an ac voltage source, whose dynamic characteristics are determined by its controller. Although different droop control implementations have been proposed in the literature, their key features are almost the same, which are the droop mechanisms between active power P and power angle δ (or angular speed ω), and between reactive power Q and inverter voltage E. Here, the RDC is adopted since it contains exactly these droop features [4], [25]. The block diagram of the RDC is shown in Fig. 2.

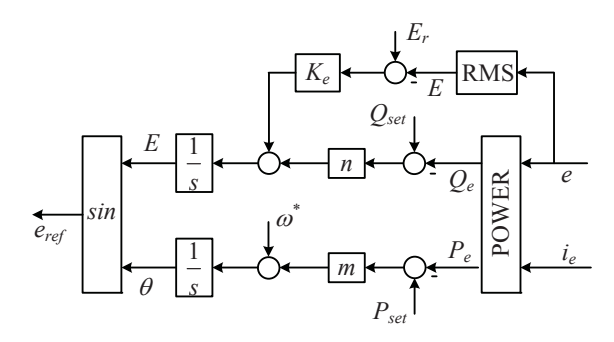


Figure 2. Block diagram of the adopted RDC.

The dynamic model of this controller is expressed as

$$\begin{cases} \dot{\delta} = m \left(P_{set} - P_e \right) + \left(\omega^* - \omega_g \right) \\ \dot{E} = n \left(Q_{set} - Q_e \right) + K_e \left(E_r - E \right) \end{cases}$$
 (2)

where $P_{set}, Q_{set}, \omega^*$ and E_r are the references of the controller, and m, n, and K_e are the droop coefficients, as shown in Table II. Besides, since it is usually considered that both ω^* and ω_g have the nominal value in the SMIB system, the term $(\omega^* - \omega_g)$ is omitted in the following sections. P_e and Q_e are the output active and reactive power of the inverter, as shown at bus 4 in Fig. 1. Considering the reduced network shown in (1), the output power of the inverter can be calculated as

$$P_e = E^2 G_{22} + E V_g X_{21} \sin \left(\delta + \varphi\right) \tag{3}$$

$$Q_e = -E^2 B_{22} - E V_q X_{21} \cos\left(\delta + \varphi\right) \tag{4}$$

where $X_{21} = \sqrt{G_{21}^2 + B_{21}^2}$, $\sin \varphi = \frac{G_{21}}{X_{21}}$, and $\cos \varphi = \frac{B_{21}}{X_{21}}$.

III. EXISTENCE OF THE FEASIBLE EQUILIBRIUM POINTS

Since transient stability investigates whether the system is able to return to a proper SEP after the disturbance, the existence of a feasible SEP should be the prerequisite of transient stability. In this section, the conditions will be derived to guarantee the SEP of the system falls within a feasible region to avoid instability, overvoltage, or overcurrent.

It can be easily found from the system dynamics (2) that at the equilibrium points, the following conditions should be met

$$\begin{cases} 0 = m (P_{set} - P_e) \\ 0 = n (Q_{set} - Q_e) + K_e (E_r - E) \end{cases}$$
 (5)

which lead to the requirements $P_e=P_{set}$ and $Q_e=Q_{set}+\frac{K_e}{n}(E_r-E)$ under the assumption that the droop coefficients m and n are nonzero. Hence, the sub-equations in (5) can be further derived as

$$\begin{cases}
EV_g X_{21} \sin \left(\delta + \varphi\right) = P_{set} - E^2 G_{22} \\
EV_g X_{21} \cos \left(\delta + \varphi\right) = -Q_{set} - \frac{K_e}{n} \left(E_r - E\right) - E^2 B_{22}
\end{cases} \tag{6}$$

where the system steady-state model (3)-(4) is taken into consideration. By squaring and adding the two sub-equations in (6) together, a quartic equation of the inverter voltage E can be obtained as an equivalent condition at the system equilibrium point, shown as

$$g(E) = \alpha E^4 + \beta E^3 + \gamma E^2 + \epsilon E + \kappa = 0 \tag{7}$$

where $\alpha=G_{22}^2+B_{22}^2$, $\beta=-\frac{2B_{22}K_e}{n}$, $\gamma=\frac{K_e^2}{n^2}+\frac{2B_{22}E_rK_e}{n}-2P_{set}G_{22}+2Q_{set}B_{22}-V_g^2X_{21}^2$, $\epsilon=-\frac{2E_rK_e^2}{n^2}-\frac{2Q_{set}K_e}{n}$, and $\kappa=P_{set}^2+Q_{set}^2+\frac{E_r^2K_e^2}{n^2}+\frac{2Q_{set}E_rK_e}{n}$. With the above preparation, the following requirements are adopted to regulate the operation of the inverter:

(1) The limits on the operation status are

$$\begin{cases}
P_{set} > 0 \\
Q_{set} + \frac{K_e E_r}{r} > 0
\end{cases}$$
(8)

which regulate the power direction of the droop controlled inverter. Note $P_{set} > 0$ is natural for an inverter, and $Q_{set} + \frac{K_e E_r}{n} > 0$ is always satisfied with the proper droop coefficients.

(2) The limits on the inverter capacity are

$$\begin{cases}
|P_{set}| < S_{max} \\
|Q_{set}| < S_{max} \\
P_e^2 + Q_e^2 < S_{max}^2
\end{cases}$$
(9)

where S_{max} is the maximal operation power of the inverter.

(3) The limits for the proper inverter voltage solution are

$$\begin{cases}
g(E_{min}) < 0 \\
g(E_{max}) > 0
\end{cases}$$
(10)

where E_{min} and E_{max} are respectively the minimal and maximal inverter voltages. These requirements guarantee the existence of a feasible inverter voltage solution within the range (E_{min}, E_{max}) , which can be further explained as follows.

It can be seen that solving the equilibrium points of the system (5) is equivalent to solving the quartic function (7) of E, which should have 4 solutions. Without loss of generality, these 4 solutions are denoted as $E_1 \sim E_4$, where $\operatorname{Re}(E_1) \geqslant \operatorname{Re}(E_2) \geqslant \operatorname{Re}(E_3) \geqslant \operatorname{Re}(E_4)$.

According to the characteristics of the coefficients, it can be found that $\alpha=G_{22}^2+B_{22}^2>0$, $\beta=-\frac{2B_{22}K_e}{n}>0$ (normally $G_{22}>0$ and $B_{22}<0$) and $\kappa=P_{set}^2+Q_{set}^2+\frac{E_r^2K_e^2}{n^2}+\frac{2Q_{set}E_rK_e}{n}>0$ (with normal droop coefficients). Therefore, the following conclusions can be obtained:

On one hand, since

$$\begin{cases} E_1 + E_2 + E_3 + E_4 = -\frac{\beta}{\alpha} < 0 \\ E_1 \cdot E_2 \cdot E_3 \cdot E_4 = \frac{\kappa}{\alpha} > 0 \end{cases}$$

it can be concluded that at least two solutions of (7) have negative real parts, where it is assumed that $\operatorname{Re}(E_1) \geqslant \operatorname{Re}(E_2) > 0$ and $0 > \operatorname{Re}(E_3) \geqslant \operatorname{Re}(E_4)$. Since the negative value is not meaningful as the voltage, only E_1 and E_2 are further discussed.

On the other hand, since $\alpha>0$ and $\kappa>0$, it can be concluded that $g\left(\infty\right)\to\infty$ and $g\left(0\right)>0$. Therefore, two scenarios exist as shown in Fig. 3. Obviously, it is hoped that $g\left(E\right)$ has two crossing points with the positive E-axis so that both E_1 and E_2 are real. Under this case, it will be shown in the following section that E_1 is the stable solution, so it is further expected that E_1 is between the pre-defined maximal and minimal values.

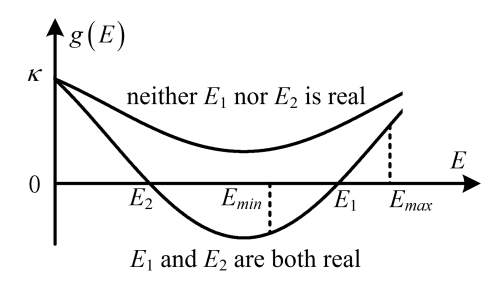


Figure 3. Illustration of the function (7) on the positive E-axis.

It is shown in Fig. 3 that as long as $g(E_{min}) < 0$ and $g(E_{max}) > 0$, g(E) is guaranteed to have two crossing points with the positive E-axis, and the inverter voltage E_1 is within the proper range. Therefore, the conditions (10) are adopted.

By combining (8)-(10), the conditions on the control references P_{set} , Q_{set} , and E_r can be obtained, which guarantee the existence of a SEP within the feasible operating region. One illustration is given in Fig. 4 for the system with the constraint limits set as $E_{max}=1.2\,\mathrm{p.u.}$, $E_{min}=0.8\,\mathrm{p.u.}$, and $S_{max}=1.0\,\mathrm{p.u.}$. During system operation, the control references should always be selected within this region to guarantee the existence of a feasible post-disturbance operating point.

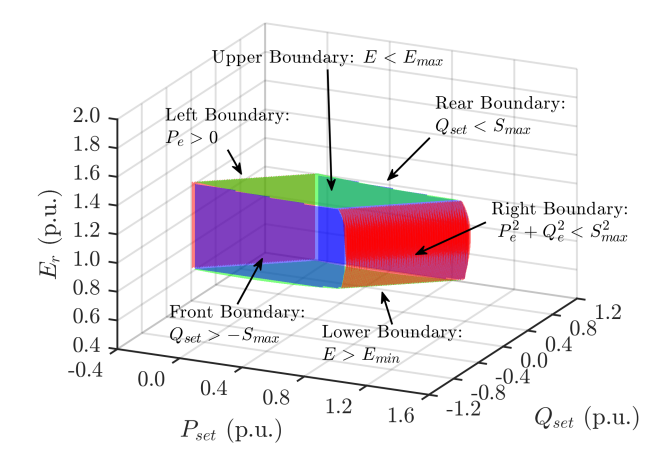


Figure 4. Illustrative feasible operation region for the control references, with the parameters shown in Tables I and II.

IV. CHARACTERIZATION OF THE EQUILIBRIUM POINTS

With the conditions proposed in Section III, the existence of the proper equilibrium points is guaranteed. In this section, these equilibrium points will be analyzed both qualitatively and quantitatively, as a preparation for the transient stability study. It should be clarified that either the qualitative method or the quantitative method can be applied individually to analyze the equilibrium points of the studied system, but together they

can provide more comprehensive perspectives to understand the problem. The qualitative analysis gives a clear visual illustration, whereas the quantitative analysis gives accurate mathematical expressions. It will be shown that the results of both methods match each other.

A. Qualitative Analysis by Nullclines

As can be seen from Section II, the system dynamic model is nonlinear due to the power flow expressions. Usually, it is almost impossible to directly and explicitly find the solutions of such a nonlinear system. However, the idea of nullclines can be adopted to help analyze the system characteristics.

For the system dynamics shown in (2), the δ -nullcline and E-nullcline are respectively defined as the set of points in the phase plane where $\dot{\delta}=0$ and $\dot{E}=0$ [27]. By combining (2)-(4) and solving the corresponding equations, the δ -nullcline of the system can be found as

$$E = \frac{-V_g X_{21} \sin(\delta + \varphi)}{2G_{22}} + \frac{\sqrt{\left[V_g X_{21} \sin(\delta + \varphi)\right]^2 + 4G_{22} P_{set}}}{2G_{22}},$$
(11)

and the E-nullcline of the system can be found as

$$E = \frac{-V_g X_{21} \cos(\delta + \varphi) + \frac{K_e}{n}}{2B_{22}} - \frac{\sqrt{\left[V_g X_{21} \cos(\delta + \varphi) - \frac{K_e}{n}\right]^2 - 4B_{22} \left(Q_{set} + \frac{K_e E_r}{n}\right)}}{2B_{22}}.$$
(12)

Note that both (11) and (12) represent the positive solutions of corresponding nullclines under the studied situation. Although both $\dot{\delta}=0$ and $\dot{E}=0$ result in quadratic equations of E, which have two solutions mathematically, only the positive solutions are meaningful because E denotes the inverter voltage which can only be positive. Under the normal parameters, there are $G_{22}>0$ and $B_{22}<0$, and thus, (11) and (12) are positive.

Based on the above calculations, the system nullclines can be illustrated in Fig. 5. Geometrically, the δ -nullcline is composed of the points where the system vectors are either straight up or down, and the E-nullcline is composed of the points where the system vectors are either straight left or right. Furthermore, in any single area divided by the nullclines, all the system vectors must point in only one of the four general directions: left-up, left-down, right-up, and right-down. These vector field directions of the system are also illustrated in Fig. 5.

It can be seen, qualitatively, from Fig. 5 that the system equilibrium points are the points where the δ -nullcline and the E-nullcline cross, which means both $\dot{\delta}=0$ and $\dot{E}=0$ are satisfied. Furthermore, the equilibrium points marked with stars in Fig. 5 should be the SEPs since in any of the areas around them, the system trajectories all flow toward them. On the other hand, the equilibrium points marked with circles in Fig. 5 should be the UEPs since in any area around them, the system trajectories all pass them by.

B. Solutions and Properties of the Equilibrium Points

As mentioned, the equilibrium points can also be mathematically obtained by solving the equations (5). There are two

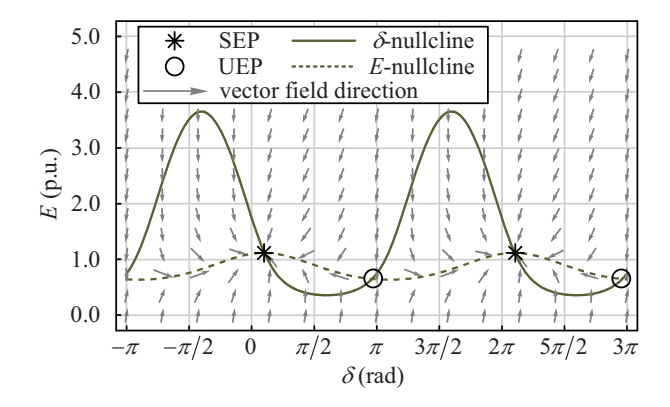


Figure 5. System nullclines, vector field directions, and equilibrium points.

categories of equilibrium points: $[E_1, \delta_1]$ with higher voltage values (stars in Fig. 5) and $[E_2, \delta_2]$ with lower voltage values (circles in Fig. 5). They can be solved as

$$\begin{cases} E_{i} = -\frac{\beta}{4\alpha} + \frac{1}{2}\sqrt{\frac{\beta^{2}}{4\alpha^{2}} - \frac{2\gamma}{3\alpha} + \Delta} \\ \pm \frac{1}{2}\sqrt{\frac{\beta^{2}}{2\alpha^{2}} - \frac{4\gamma}{3\alpha} - \Delta + \frac{-\frac{\beta^{3}}{\alpha^{3}} + \frac{4\beta\gamma}{\alpha^{2}} - \frac{8\epsilon}{\alpha}}{4\sqrt{\frac{\beta^{2}}{4\alpha^{2}} - \frac{2\gamma}{3\alpha} + \Delta}}} \\ \delta_{i} = \arccos\frac{-Q_{set} - \frac{K_{e}}{n}(E_{r} - E_{i}) - E_{i}^{2}B_{22}}{E_{i}V_{g}X_{21}} - \varphi + 2k\pi, \end{cases}$$

$$(13)$$

where i=1, 2 and $k \in \mathbb{Z}$. E_1 takes the plus sign on its second row and E_2 takes the minus sign. Furthermore, there is

$$\Delta = \frac{\sqrt[3]{2}\Delta_1}{3\alpha\sqrt[3]{\Delta_2 + \sqrt{-4\Delta_1^3 + \Delta_2^2}}} + \frac{\sqrt[3]{\Delta_2 + \sqrt{-4\Delta_1^3 + \Delta_2^2}}}{3\sqrt[3]{2}\alpha}$$

with $\Delta_1 = \gamma^2 - 3\beta\epsilon + 12\alpha\kappa$, and $\Delta_2 = 2\gamma^3 - 9\beta\gamma\epsilon + 27\alpha\epsilon^2 + 27\beta^2\kappa - 72\alpha\gamma\kappa$. It is clear that the equilibrium points are periodic along the δ -axis with a 2π period.

The properties of the equilibrium points can be further mathematically verified by calculating the eigenvalues of the corresponding Jacobian matrix. According to the system dynamics (2), the expression of the Jacobian matrix is shown in (14), and its eigenvalues λ_1 and λ_2 are given by

$$\lambda_{1} = \frac{J_{\delta\delta} + J_{EE} - \sqrt{(J_{\delta\delta} + J_{EE})^{2} - 4(J_{\delta\delta}J_{EE} - J_{\delta E}J_{E\delta})}}{\frac{2}{2}}$$

$$\lambda_{2} = \frac{J_{\delta\delta} + J_{EE} + \sqrt{(J_{\delta\delta} + J_{EE})^{2} - 4(J_{\delta\delta}J_{EE} - J_{\delta E}J_{E\delta})}}{2}$$
(15)

The corresponding eigenvectors of λ_1 and λ_2 are respectively expressed by η_1 and η_2 as

$$\eta_1 = \begin{bmatrix} \frac{\lambda_1 - J_{EE}}{J_{E\delta}} \\ 1 \end{bmatrix}, \quad \eta_2 = \begin{bmatrix} \frac{\lambda_2 - J_{EE}}{J_{E\delta}} \\ 1 \end{bmatrix}$$
 (16)

With the above derivations, the stability property of an equilibrium point can be determined by substituting its expression into (14)-(15), and examining the corresponding eigenvalues: if both

 $\operatorname{Re}(\lambda_1)$ and $\operatorname{Re}(\lambda_2)$ are negative, then the equilibrium point is a SEP. Otherwise, the equilibrium point is a UEP [28]. These quantitative discussions of the system equilibrium points match with the observations from Fig. 5.

V. TRANSIENT STABILITY STUDY AND VERIFICATION

With the derived post-disturbance equilibrium points, the system transient angle stability will be further investigated in this section by exploring the stability boundaries and attraction regions of the SEPs. In this work, the theorem 3.15 in [29] is adopted, which describes the characteristics of the stability boundaries of the SEPs:

- 1) One UEP is on the stability boundary of a SEP, if and only if the unstable manifolds of this UEP contain the trajectories flowing to the above SEP.
- 2) The stability boundary of a SEP is formed by the union of the stable manifolds of all the UEPs, which are located on the stability boundary of this SEP.

Based on this theorem, the stability boundary of one SEP can be obtained by: 1) finding the surrounding UEPs which are on the stability boundary of this SEP, and 2) finding the union of the stable manifolds of these UEPs. These steps will be conducted in this section to determine the attraction region of the studied system, and the system transient stability characteristics will be further discussed.

A. Characterization of the Attraction Region

1) UEPs on the Stability Boundary: As mentioned, the first step to obtain the stability boundary of a SEP is to determine the UEPs on the stability boundary. According to the previous discussions, it has been found that there is only one pair of SEP and UEP within one 2π period along the δ -axis. Therefore, it is reasonable to infer that this UEP should be on the stability boundary of the corresponding SEP since there is no other option. This inference can be easily verified through an illustration in Fig. 6, since the plotted unstable manifolds of the UEPs indeed contain the trajectories flowing to the SEPs.

Based on the above confirmation, the next step, which is also the key in our analysis, is to find the stable manifolds of the UEPs, which are obtained by the trajectories starting from the UEPs, taking the directions of their stable eigenvectors, and flowing backward in time. In this work, the stable manifolds of these UEPs will be acquired respectively by the following two methods:

- The first method is the numerical integration, which is conducted by Euler method in this work [26]. The stable manifolds obtained by this method will be denoted as the numerical ones, and they will be regarded as accurate results because they are calculated step by step directly from the system dynamic model.
- 2) The second method, which will be further explained as follows, is the analytical approximation where an analytical expression will be derived to approximate the stable manifolds of the UEPs. The results obtained by this method will be denoted as the analytical ones in this work.

As is well known, the numerical integration method is generic and can be applied to any systems with a clear dynamic model, but cannot lead to analytical results. In this work, these two methods will be respectively conducted and compared, and it

$$\boldsymbol{J} = \begin{bmatrix} J_{\delta\delta} & J_{\delta E} \\ J_{E\delta} & J_{EE} \end{bmatrix} = \begin{bmatrix} -mEV_gX_{21}\cos\left(\delta + \varphi\right) & -2mEG_{22} - mV_gX_{21}\sin\left(\delta + \varphi\right) \\ -nEV_gX_{21}\sin\left(\delta + \varphi\right) & 2nEB_{22} + nV_gX_{21}\cos\left(\delta + \varphi\right) - K_e \end{bmatrix}$$
(14)

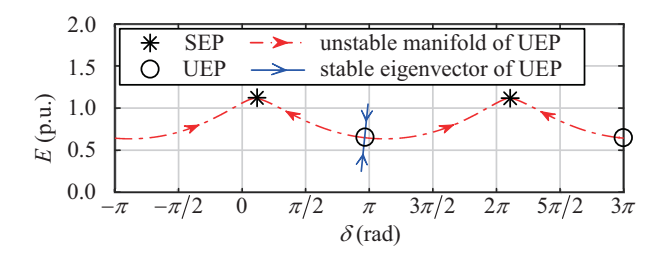


Figure 6. The unstable manifolds and the stable eigenvectors of the UEPs.

will be demonstrated that the analytical approximation of the stable manifolds is precise enough to represent the results of the numerical integration.

2) Analytical Approximation of the Stable Manifolds: It is known that the stable manifolds close to one UEP itself take the direction of the stable eigenvectors, as shown in Fig. 6. However, it is unknown how these stable manifolds flow farther in the phase plane.

To answer the above question, the system nullclines obtained in Section IV-A are introduced again, as shown in Fig. 7. It can be seen that in all of the areas above the E-nullcline, the system vector field points to the negative E direction. And in all of the areas below the E-nullcline, the vector field points to the positive E direction. That is, if one starts from the discussed UEP, takes its stable eigenvector direction, and integrates backward in time, then the obtained stable manifold will extend along with the vector field direction.

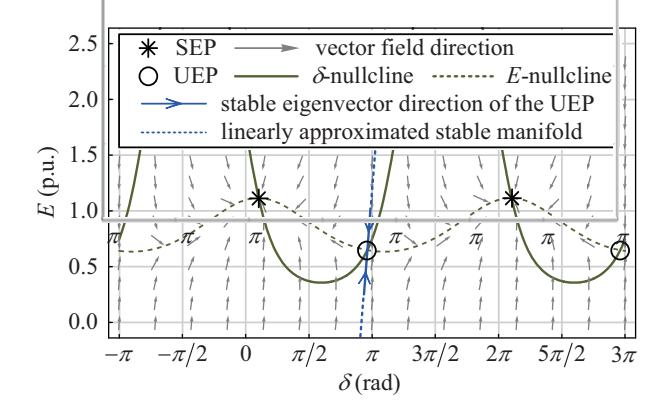


Figure 7. The nullclines, stable eigenvector direction, and approximated stable manifold of the UEP.

According to the above analysis, it can be concluded that the stable manifolds of the UEP should have a nearly linear shape in the phase plane, and therefore, it becomes more reasonable to linearly approximate these stable manifolds compared to the scenario where the stable manifolds would turn around as they flow. In this work, the stable eigenspace of a UEP is adopted to approximate its stable manifolds, which is the span of the stable eigenvector, as shown in Fig. 7. Furthermore, since the position of stable eigenspace is used to represent the stability boundary of the SEP, only the slope of the stable eigenspace is needed to

form a linear function $E = f_s(\delta)$, and to express the position of the stability boundary.

Based on the system eigenvalues (15), it can be seen that for the UEP, there is $\lambda_1 < 0$ and $\lambda_2 > 0$ since there is a minus sign in λ_1 and a plus sign in λ_2 . Therefore, η_1 is the stable eigenvector. Considering one specific UEP as $\left[\overline{E}_2, \overline{\delta}_2\right]$, the slope of η_1 can be obtained according to (16) and the position of the stable eigenspace is then expressed as

$$E = f_s(\delta) = \frac{J_{E\delta}}{\lambda_1 - J_{EE}} \left(\delta - \overline{\delta}_2 \right) + \overline{E}_2 \tag{17}$$

where λ_1 , $J_{E\delta}$ and J_{EE} are the eigenvalue and Jacobian matrix elements corresponding to this specific UEP. Therefore, (17) offers an analytical form of the stable manifold, in contrary to the result obtained through numerical integration.

3) Comparison and Validation: The illustration of stable manifolds of the UEPs is depicted in Fig. 8, with the analytical ones determined according to (17) and the numerical ones obtained through the numerical integration directly. According to Fig. 8, both results match very well. Furthermore, considering the stability boundary of each SEP is the union of the stable manifolds of the surrounding UEPs, it can be concluded that the attraction region of each SEP is the belt area shown in Fig. 8.

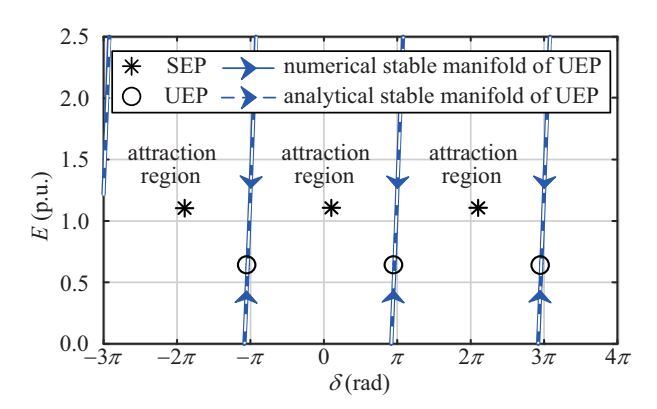


Figure 8. Numerical stable manifolds of the UEPs marked by thick solid lines, and analytical stable manifolds of the UEPs marked by dashed lines.

B. Transient Stability Characteristic

Since the attraction regions of the SEPs are closely next to each other in Fig. 8, it can be speculated that the system trajectory will always fall into the attraction region of one of the SEPs. Considering the system is originally operated at one SEP (usually it is thought as the one where $0 \le \delta \le \frac{\pi}{2}$), then it can be concluded that there are only two scenarios regarding the post-disturbance system, which can be respectively described as:

- During the disturbance, the system trajectory stays within the attraction region of the original operating point and therefore, will return to this SEP after the disturbance.
- During the disturbance, the system trajectory flows beyond the attraction region of the original operating point and therefore, will be attracted by a neighboring SEP.

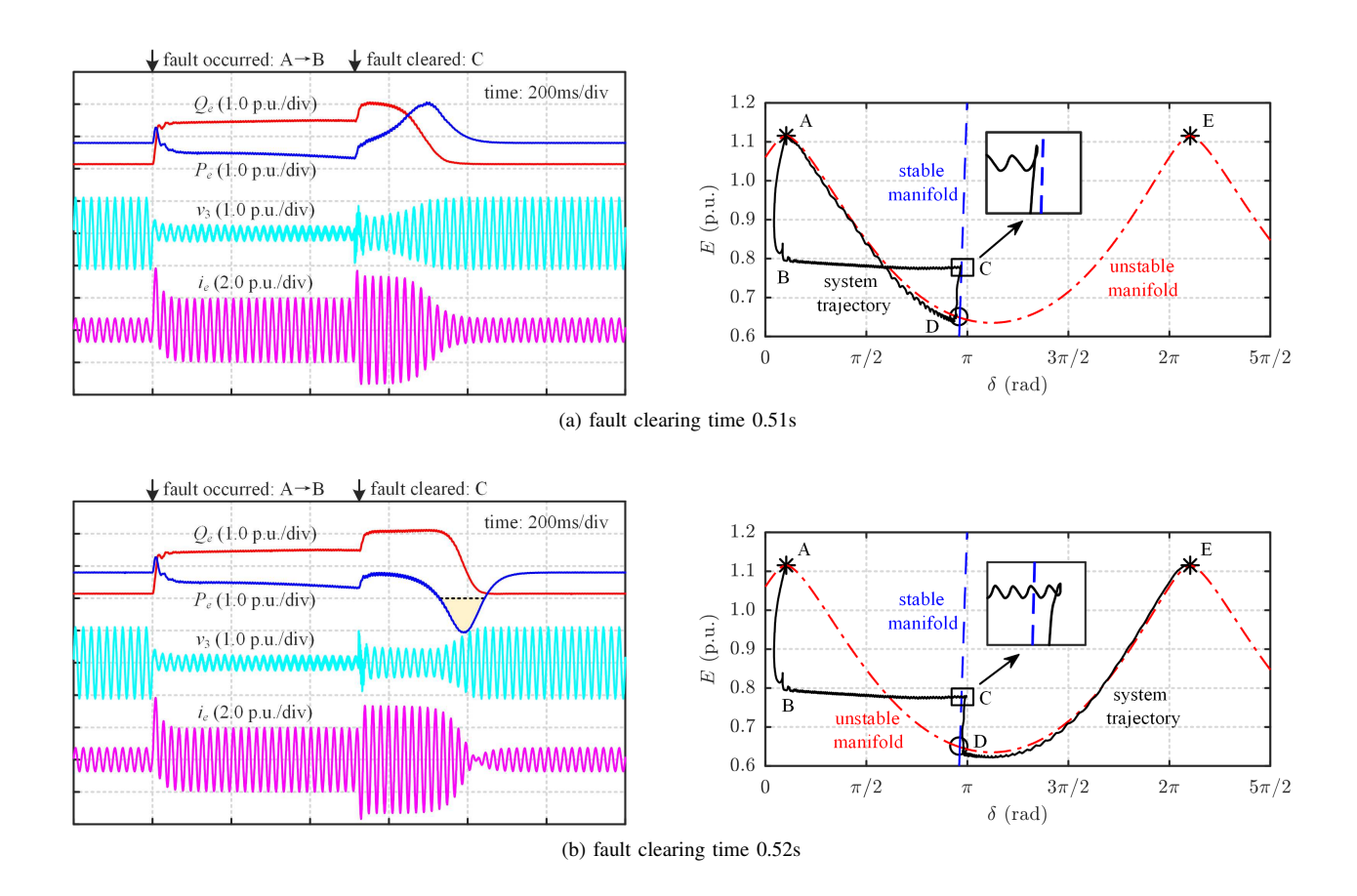


Figure 9. Inverter transient responses (left column) and system phase portraits (right column) under different fault clearing times.

Both the above-mentioned scenarios end up with a stable operating point, therefore, it can be considered that the droop controlled inverter has a good transient stability characteristic from the perspective of its final operation state. Furthermore, the reverse active power phenomenon may occur in the post-disturbance system, especially in the second case, which will be further discussed in Section VI.

C. Simulation Verification

To verify the above-mentioned conclusions, simulations are carried out with the studied system shown in Fig. 1. Considering the system is operated under the normal condition when the fault occurs, the inverter transient responses and system phase portraits are shown in Fig. 9 with different fault clearing times.

- 1) Fault Clearing Time 0.51s. The inverter transient responses (the output power, terminal voltage, and output current) and the system phase portrait are shown in Fig. 9(a) when the fault clearing time is 0.51s. In the phase portrait, the system trajectory stays at the original SEP A during normal operation, moves to state point B at the time of fault occurrence, and further to state point C during the fault. The fault is cleared at point C. Since the trajectory around point C stays within the attraction region of the SEP A, the following trajectory is attracted by this SEP and returns to it.
- 2) Fault Clearing Time 0.52s: When the fault clearing time increases to 0.52s, the inverter transient responses and the system phase portrait are respectively shown in Fig. 9(b). Similarly, the fault is also cleared at state point C in the phase portrait. It can be seen that since the trajectory around point C has already

gone out of the attraction region of the SEP A and flowed to the neighboring operation region, the following trajectory is attracted by the neighboring SEP at point E.

Under both cases, the system is able to eventually return to a stable operating state after the disturbance. However, when the clearing time is 0.52s, the reverse active power occurs during the post-disturbance dynamics, as shown in Fig. 9(b), which is consistent with the discussions above. Furthermore, another observation can be made in Fig. 9 that after the fault clearing, the post-disturbance trajectory tends to move along with the unstable manifold of the corresponding UEP when it is attracted by the SEP. This characteristic can also be qualitatively observed from the system vector field shown in Fig. 5, and may be used to analyze the operation of the post-disturbance system. For example, since the post-disturbance trajectory tends to move along with the unstable manifold in Fig. 9, there is a decrease for inverter voltage E and an increase for inverter power P_e and Q_e at the fault clearing moment, and therefore, the inverter current i_e further increases after the fault is cleared, as shown in Fig. 9.

VI. TRANSIENT CONTROL CONSIDERATION

The transient angle stability of droop controlled inverters has been discussed in the previous sections. However, two remaining concerns should be further addressed considering the practical operation of inverters. Firstly, since the inverter is not able to endure a large current like a conventional synchronous generator, it has to be equipped with the current limiting scheme to ridethrough the disturbance and avoid overcurrent damaging. And secondly, the above-mentioned reverse active power phenomenon

in Section V-B needs to be investigated regarding its cause and prevention. Therefore, the additional transient control considerations are discussed in this section to further maintain the transient stability characteristics of droop controlled inverters.

A. Current Limiting Control

Regarding the current limiting control, it should be noticed that a proper scheme should only protect the inverter during the transient process, but not affect its normal operation. Some current limiting methods have been proposed in the literature, such as the use of limiters in the current control loop [30], [31], the direct adjustment of the PWM reference signal [32], and the adoption of virtual impedance [33], [34]. Among them, the adoption of virtual impedance is a flexible technique suitable for voltage source controllers.

Therefore, a virtual impedance based current limiting scheme is implemented in this subsection, as shown in Fig. 10. Considering e_{ref} as the voltage reference generated by the original droop controller in Fig. 2, then the actual reference signal for the PWM generator v_r is controlled as (18).

$$v_r = e_{ref} - R_{vir} \cdot i_e \tag{18}$$

where R_{vir} is the generated virtual resistance.

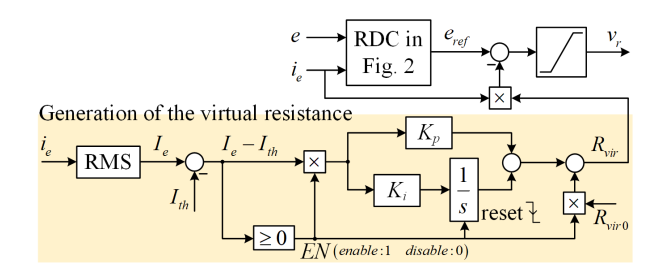


Figure 10. Generation of the virtual impedance for current limiting.

In this scheme, the RMS (or magnitude) value of the inverter output current is measured as I_e , and compared with the threshold I_{th} to generate the virtual resistance R_{vir} as

$$R_{vir} = \begin{cases} 0 & I_{e} < I_{th} \\ R_{vir0} + K_{p} (I_{e} - I_{th}) + K_{i} \int_{0}^{t} (I_{e} - I_{th}) dt & I_{e} \ge I_{th} \end{cases}$$
(19)

Under normal operation when I_e is smaller than I_{th} , the PI controller is disabled and therefore, the virtual resistance $R_{vir}=0$, which does not affect the original controller as $v_r=e_{ref}$. When a fault occurs and the terminal voltage drops, a large current will be produced and a virtual resistance will be quickly generated according to (19). In this way, the inverter output voltage and current will be limited to prevent it from damage.

Further consideration should be taken into account when the current limiting scheme is implemented since the virtual impedance also equivalently changes the system topology. Considering the post-disturbance state indicates the system has returned to its normal structure and control, it should be noticed that when the current limiting is implemented, the post-disturbance system is the one where the fault has been cleared and the current saturation has ended, i.e., R_{vir} becomes zero. Therefore, the post-disturbance system is under the completely

normal operation, which in this work, can be described by the pre-disturbance system model in Section II.

B. Reverse Active Power Phenomenon

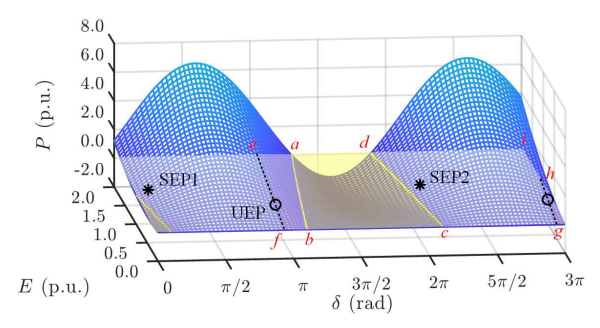
As shown in Fig. 9(b) in Section V-C, the reverse active power phenomenon may occur in the post-disturbance system, especially when the trajectory is attracted by the neighboring SEP. This phenomenon can be explained by the $P(\delta, E)$ surface of the post-disturbance system shown in Fig. 11(a), which is obtained according to the system active power equation (3). It can be seen that as long as the post-disturbance system states (δ, E) fall within the yellow-colored area marked by abcd, the active power value will become negative, meaning a reversed direction. This reverse active power area can be found by solving

$$P(\delta, E) = E^2 G_{22} + E V_g X_{21} \sin(\delta + \varphi) < 0.$$
 (20)

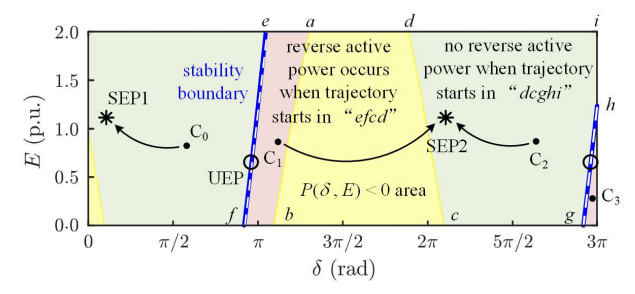
It should be noticed that since the system dynamics are periodic along the δ axis with a 2π period, this reverse active power area also appears periodically. In this work, the specific area marked by abcd is focused. According to Fig. 11(a), the cause of the reverse active power phenomenon can be explained in the system phase plane shown in Fig. 11(b).

In Fig. 11(b), considering the scenario where the system is originally operated at SEP1 before the disturbance, the trajectory flows to the right side of the stability boundary during the disturbance and is attracted by the neighboring SEP2 in the post-disturbance system. If the fault is cleared so that the postdisturbance trajectory starts from the red-and-yellow-colored area denoted by efcd, for example starting from point C_1 , then during the process that the trajectory flows from C₁ to the postdisturbance SEP2, it will go through the area abcd, leading to the reserve active power. On the contrary, if the fault is cleared so that the post-disturbance trajectory starts from the green-colored area denoted by dcghi, for example starting from point C_2 , then the trajectory will not enter the reverse active power area during the post-disturbance dynamics, and no reserve active power will occur under this circumstance. The same analysis can be applied to each SEP with the 2π interval. For example, if the postdisturbance trajectory starts from point C_0 , then it will flow back to the original SEP1, where the reverse active power will not occur. And if the post-disturbance trajectory starts from point C₃, then it will be attracted to the next SEP on the farther right, and the reverse active power phenomenon will occur again.

In order to deal with this reverse active power phenomenon, a hardware approach is to implement proper dc side storage to the inverter, so that the bidirectional active power is allowed. On the other hand, this phenomenon can also be prevented from the perspective of control. For example, considering ideally that the system state can be monitored during operation, if it is found the system state has already moved beyond the attraction region of the original SEP1 and will be attracted by a neighboring SEP2, then the fault clearing time can be intentionally delayed to a proper value so that the system trajectory can fully pass the reverse active power area during the fault, and the post-disturbance trajectory can start from the green-colored area. Under this circumstance, the post-disturbance trajectory will not enter the reverse active power area, and the corresponding phenomenon can be avoided.



(a) $P\left(\delta,E\right)$ surface of the post-disturbance system



(b) post-disturbance trajectory movements with different starting points

Figure 11. Characteristics of the post-disturbance system regarding the reverse active power phenomenon.

C. Simulation Results

In this subsection, simulations are carried out regarding the current limiting scheme and reverse active power phenomenon. The system parameters remain unchanged, and the threshold for the current value is set as 1.50 p.u.. Similar to Fig. 9, different cases are also tested when the three-phase fault is cleared respectively after different times. The results are shown in Fig. 12. It can be seen that with the current limiting scheme, the inverter current is properly regulated within the tolerable range after the fault occurs in all cases. And when the fault is cleared, the system can all finally return to the normal operation state, which means the analysis in the previous sections can still be maintained. Furthermore, with different fault clearing times, the system demonstrates different transient responses, which can be elaborated as follows.

1) Fault Clearing Time 0.15s: The system responses when the fault is cleared at 0.15s are shown in Fig. 12(a), which is corresponding to the case of point C_0 in Fig. 11(b).

In this case, the fault clearing point C stays within the attraction region of SEP A. After the fault is cleared, the inverter current keeps saturated for some time, and finally, the trajectory returns to the original SEP at point A. During all this process, the system trajectory remains in the green-colored area and therefore, no reverse active power occurs under this circumstance. Note that there is a visible delay for the current to desaturate.

2) Fault Clearing Time 0.51s: The system responses when the fault is cleared at 0.51s are shown in Fig. 12(b), which is corresponding to the case of point C_1 in Fig. 11(b).

While the behavior is expected to be similar to that in Fig. 9(a), the current limiting mechanism changes the system behavior and causes the system dynamics to escape from the attraction region of the original SEP during the fault. The system is attracted by the next SEP at point D, leading to the reverse active power.

3) Fault Clearing Time 1.22s: The system responses when the fault is cleared at 1.22s are shown in Fig. 12(c), which is corresponding to the case of point C_2 in Fig. 11(b).

Under this circumstance, the fault is cleared and the inverter exits the current saturation at the same time, where the system trajectory has already fully passed the $P\left(\delta,E\right)<0$ area and entered the green-colored area. Then the post-disturbance trajectory is attracted to the neighboring SEP at point D without going through the reverse active power area, and therefore, the reverse active power phenomenon is avoided.

4) Fault Clearing Time 1.64s: The system responses when the fault is cleared at 1.64s are shown in Fig. 12(d), which is corresponding to the case of point C_3 in Fig. 11(b).

When the fault clearing time is 1.64s, the system trajectory moves so far that it has escaped from the attraction region of the SEP at point D, and entered the attraction region of the farther SEP at point E. Similar to Fig. 12(b), the fault is cleared at point C and the inverter exits current saturation after a short time, both in the corresponding red-and-yellow-colored area in this period. Therefore, the post-disturbance trajectory is attracted to point E, and the reverse active power occurs again.

The above simulation results further validate the discussions in this section. On one hand, the current limiting control protects the inverter from overcurrent during the transient process. And on the other hand, the reverse active power phenomenon can be prevented by the proper selection of fault clearing time. With these control considerations, the transient stability characteristics can be better guaranteed for droop controlled inverters. At the same time, it should be recognized that the current limiting scheme can profoundly affect the system dynamics during the fault and after it is cleared. With some fault clearing points, even the fault is cleared in the green-colored area, but the current limiting may cause the system dynamics to enter the red-andyellow-colored area and therefore, the actual post-disturbance trajectory starts from the red-and-yellow-colored area and the reverse active power still appears. This phenomenon is related to the operation characteristics of the system after the fault is cleared, and more investigation is needed to reveal the properties and influence of the current limiting scheme and the postdisturbance system, which will be discussed in the future works.

VII. CONCLUSION

In this work, the transient angle stability of the droop controlled inverter after a large disturbance are discussed in detail. In order to guarantee that there exists a proper post-disturbance operating point, the feasible operation region for the control references is obtained. Under the circumstance where there exist feasible SEPs, the system equilibrium points are analyzed in detail. Furthermore, the attraction regions of the SEPs are accurately obtained by depicting the stable and unstable manifolds of the surrounding UEPs, which shows that the droop controlled inverter has a good transient stability characteristic since a stable operating point can always be found by the post-disturbance system. To further guarantee that the inverter can ride-through the disturbance, a current limiting scheme is implemented and the reverse active power phenomenon is discussed regarding its cause and prevention. It is shown that these transient control considerations can better guarantee the stability characteristics of the droop controlled inverters.

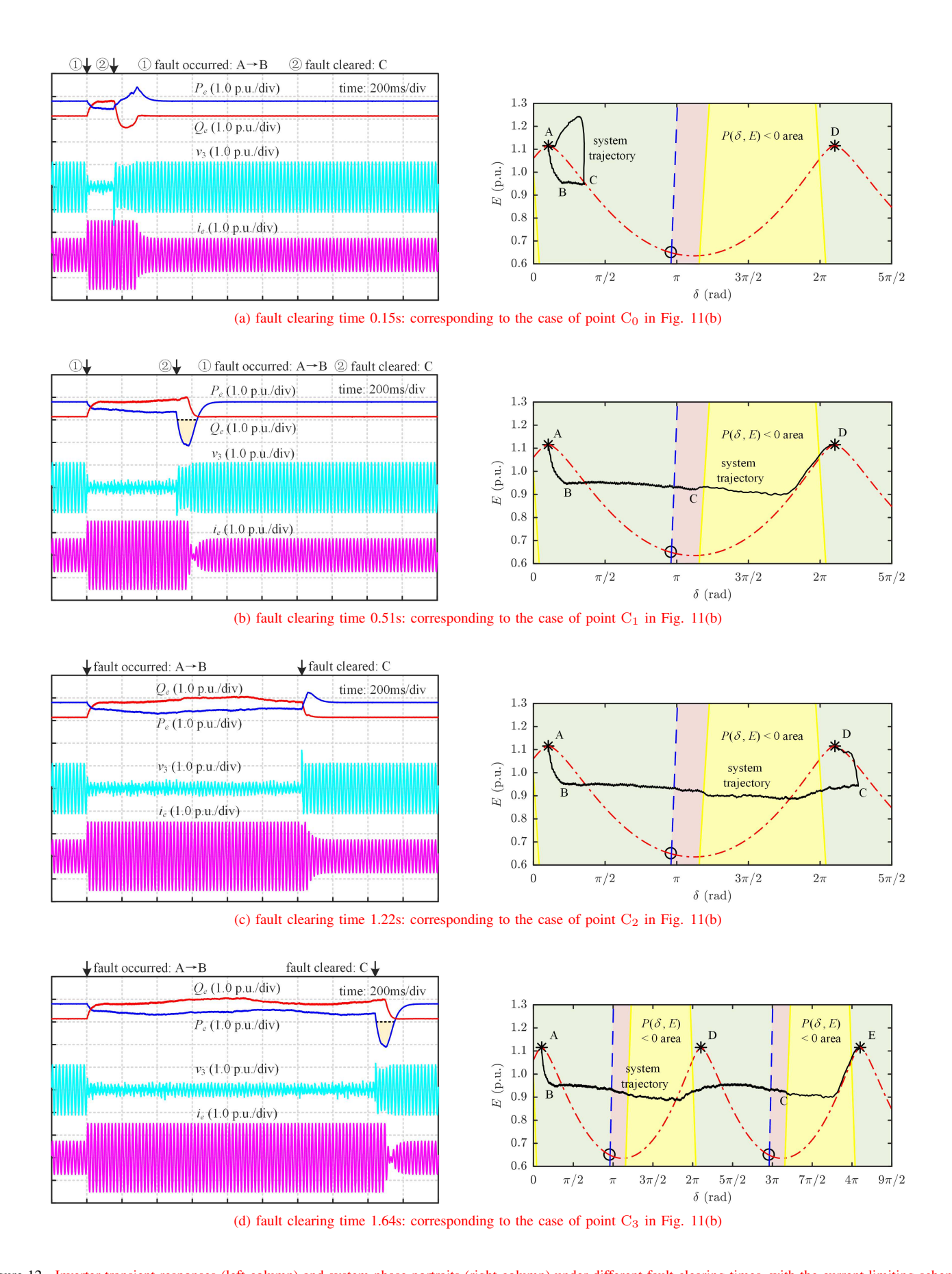


Figure 12. Inverter transient responses (left column) and system phase portraits (right column) under different fault clearing times, with the current limiting scheme.

This work intends to provide a complete explanation for the transient angle stability of inverters with the droop mechanism.

The results show that these inverters are robust regarding the transient angle stability if proper control settings are implemented.

Furthermore, the analysis method in this work can also be applied to study the transient angle stability of other kinds of voltage source inverters, such as a virtual synchronous machine with a higher-order model.

REFERENCES

- [1] Q.-C. Zhong, Power Electronics-Enabled Autonomous Power Systems: Next Generation Smart Grids. John Wiley & Sons, 2020.
- [2] P. Pinson, L. Mitridati, C. Ordoudis, and J. Ostergaard, "Towards fully renewable energy systems: Experience and trends in denmark," CSEE Journal of Power and Energy Systems, vol. 3, no. 1, pp. 26–35, March 2017.
- [3] Q.-C. Zhong, "Power-electronics-enabled autonomous power systems: Architecture and technical routes," *IEEE Transactions on Industrial Electron*ics, vol. 64, no. 7, pp. 5907–5918, July 2017.
- [4] Q.-C. Zhong and T. Hornik, Control of power inverters in renewable energy and smart grid integration. John Wiley & Sons, 2012.
- [5] Y. A. I. Mohamed and E. F. El-Saadany, "Adaptive decentralized droop controller to preserve power sharing stability of paralleled inverters in distributed generation microgrids," *IEEE Transactions on Power Electronics*, vol. 23, no. 6, pp. 2806–2816, 2008.
- [6] S. Haider, G. Li, and K. Wang, "A dual control strategy for power sharing improvement in islanded mode of ac microgrid," *Protection and Control of Modern Power Systems*, vol. 3, no. 1, p. 10, 2018.
- [7] J. Liu, Y. Miura, and T. Ise, "Comparison of dynamic characteristics between virtual synchronous generator and droop control in inverter-based distributed generators," *IEEE Transactions on Power Electronics*, vol. 31, no. 5, pp. 3600–3611, May 2016.
- [8] R. Wang, L. Chen, T. Zheng, and S. Mei, "VSG-based adaptive droop control for frequency and active power regulation in the mtdc system," *CSEE Journal of Power and Energy Systems*, vol. 3, no. 3, pp. 260–268, Sep. 2017.
- [9] Q.-C. Zhong, W. Ming, and Y. Zeng, "Self-synchronized universal droop controller," *IEEE Access*, vol. 4, pp. 7145–7153, 2016.
- [10] Q.-C. Zhong and D. Boroyevich, "Structural resemblance between droop controllers and phase-locked loops," *IEEE Access*, vol. 4, pp. 5733–5741, 2016.
- [11] P. Kundur, J. Paserba, V. Ajjarapu, G. Andersson, A. Bose, C. Canizares, N. Hatziargyriou, D. Hill, A. Stankovic, C. Taylor, T. V. Cutsem, and V. Vittal, "Definition and classification of power system stability ieee/cigre joint task force on stability terms and definitions," *IEEE Transactions on Power Systems*, vol. 19, no. 3, pp. 1387–1401, Aug 2004.
- [12] P. Piya, M. Ebrahimi, M. Karimi-Ghartemani, and S. A. Khajehoddin, "Fault ride-through capability of voltage-controlled inverters," *IEEE Transactions on Industrial Electronics*, vol. 65, no. 10, pp. 7933–7943, 2018.
- [13] I. Sadeghkhani, M. E. H. Golshan, J. M. Guerrero, and A. Mehrizi-Sani, "A current limiting strategy to improve fault ride-through of inverter interfaced autonomous microgrids," *IEEE Transactions on Smart Grid*, vol. 8, no. 5, pp. 2138–2148, Sep. 2017.
- [14] P. W. Sauer and M. A. Pai, *Power system dynamics and stability*. Prentice hall Upper Saddle River, NJ, 1998, vol. 101.
- [15] Y. Xue, T. V. Custem, and M. Ribbens-Pavella, "Extended equal area criterion justifications, generalizations, applications," *IEEE Transactions on Power Systems*, vol. 4, no. 1, pp. 44–52, Feb 1989.
- [16] X. Chen, W. Pei, and X. Tang, "Transient stability analyses of micro-grids with multiple distributed generations," in 2010 International Conference on Power System Technology, Oct 2010, pp. 1–8.
- [17] P. Hart and B. Lesieutre, "Energy function for a grid-tied, droop-controlled inverter," in 2014 North American Power Symposium (NAPS), Sept 2014, pp. 1–6.
- [18] M. Kabalan, P. Singh, and D. Niebur, "Nonlinear lyapunov stability analysis of seven models of a dc/ac droop controlled inverter connected to an infinite bus," *IEEE Transactions on Smart Grid*, pp. 1–1, 2018.
- [19] H. Xin, L. Huang, L. Zhang, Z. Wang, and J. Hu, "Synchronous instability mechanism of p-f droop-controlled voltage source converter caused by current saturation," *IEEE Transactions on Power Systems*, vol. 31, no. 6, pp. 5206–5207, Nov 2016.
- [20] J. W. Simpson-Porco, F. Dörfler, and F. Bullo, "Synchronization and power sharing for droop-controlled inverters in islanded microgrids," *Automatica*, vol. 49, no. 9, pp. 2603 – 2611, 2013.
- [21] J. Schiffer, R. Ortega, A. Astolfi, J. Raisch, and T. Sezi, "Conditions for stability of droop-controlled inverter-based microgrids," *Automatica*, vol. 50, no. 10, pp. 2457 2469, 2014.
- [22] Y. Zhang and L. Xie, "A transient stability assessment framework in power electronic-interfaced distribution systems," *IEEE Transactions on Power Systems*, vol. 31, no. 6, pp. 5106–5114, Nov 2016.

- [23] Z. Wang and M. Lemmon, "Stability analysis of weak rural electrification microgrids with droop-controlled rotational and electronic distributed generators," in 2015 IEEE Power Energy Society General Meeting, July 2015, pp. 1–5.
- [24] C. Ren, Y. Xu, and Y. Zhang, "Post-disturbance transient stability assessment of power systems towards optimal accuracy-speed tradeoff," Protection and Control of Modern Power Systems, vol. 3, no. 1, p. 19, 2018
- [25] Q.-C. Zhong, "Robust droop controller for accurate proportional load sharing among inverters operated in parallel," *IEEE Transactions on Industrial Electronics*, vol. 60, no. 4, pp. 1281–1290, 2013.
- [26] M. L. Crow, Computational methods for electric power systems. CRC Press, 2015.
- [27] M. W. Hirsch, S. Smale, and R. L. Devaney, Differential equations, dynamical systems, and an introduction to chaos. Academic press, 2004.
- [28] P. Kundur, *Power system stability and control*. McGraw-hill New York, 1994.
- [29] H.-D. Chiang, Direct methods for stability analysis of electric power systems: theoretical foundation, BCU methodologies, and applications. John Wiley & Sons, 2011.
- [30] N. Bottrell and T. C. Green, "Comparison of current-limiting strategies during fault ride-through of inverters to prevent latch-up and wind-up," *IEEE Transactions on Power Electronics*, vol. 29, no. 7, pp. 3786–3797, July 2014.
- [31] L. Huang, H. Xin, Z. Wang, L. Zhang, K. Wu, and J. Hu, "Transient stability analysis and control design of droop-controlled voltage source converters considering current limitation," *IEEE Transactions on Smart Grid*, vol. 10, no. 1, pp. 578–591, Jan 2019.
- [32] A. H. Etemadi and R. Iravani, "Overcurrent and overload protection of directly voltage-controlled distributed resources in a microgrid," *IEEE Transactions on Industrial Electronics*, vol. 60, no. 12, pp. 5629–5638, Dec 2013.
- [33] A. D. Paquette and D. M. Divan, "Virtual impedance current limiting for inverters in microgrids with synchronous generators," *IEEE Transactions* on *Industry Applications*, vol. 51, no. 2, pp. 1630–1638, March 2015.
- [34] X. Wang, Y. W. Li, F. Blaabjerg, and P. C. Loh, "Virtual-impedance-based control for voltage-source and current-source converters," *IEEE Transactions on Power Electronics*, vol. 30, no. 12, pp. 7019–7037, Dec 2015.